Optics and Laser Technology 129 (2020) 106280

Contents lists available at ScienceDirect

Optics and Laser Technology

journal homepage: www.elsevier.com/locate/optlastec

# In-process measurement of melt pool cross-sectional geometry and grain orientation in a laser directed energy deposition additive manufacturing process

Zhe Sun, Wei Guo, Lin Li*

*Laser Processing Research Centre, Department of Mechanical, Aerospace and Civil, Engineering, The University of Manchester, Manchester M13 9PL, UK*

## HIGHLIGHTS

- In-process monitoring of melt pool cross sectional geometry in a high rate deposition laser direct energy deposition process.
- In-process monitoring of material solidification grain growth directions.
- These have been verified by experiments with over 90% accuracy.

## ARTICLE INFO

*Keywords:*
Laser directed energy deposition
Laser additive manufacturing
Melt pool dimension
Track geometry
Grain growth

## ABSTRACT

Understanding the behaviour of melt pool during laser directed energy deposition (L-DED) is essential for the prediction and control of process quality. Previous effort was focused on the observation of melt pool surface characteristics. In this paper, a coaxial imaging system was employed to determine the melt pool cross sectional geometry and to predict solidified grain orientation during a high deposition rate L-DED process. The image processing procedure, deposition track cross-sectional profile prediction and the relationship between melt pool shape and melt pool dynamics, and grain growth orientation were investigated. Results show that sharp melt pool edges can be obtained so that melt pool width can be predicted with an accuracy of more than 95%. The estimation method of melt pool length has an accuracy of 90%. With the experimental melt pool width and depth data, the cross-sectional profiles of deposited track are predicted at an accuracy of 92% and a good match with experimental data is obtained. The melt pool formation is found to be able to allow the prediction of crystal growth directions during solidification.

## 1. Introduction

Laser directed energy deposition (L-DED) is a near net shape additive manufacturing process that fabricates three-dimensional parts layer-by-layer. This technique utilises a laser beam to generate a melt pool on the substrate or the previously formed layer and simultaneously melts the feedstock material which is being delivered into the melt pool in the form of a power stream or wire, either coaxially to the laser beam or off-axis. Typical applications of L-DED include surface cladding, additive manufacturing and repair of metallic components. Many studies have been carried out on L-DED process including the influence of the processing parameters on deposited track geometry and the elimination of defects, as well as the microstructural characteristics and properties of the deposited layers or additive manufactured parts.

To achieve a higher deposition rate and higher powder utilisation efficiency, some previous investigations on high deposition rate laser directed energy deposition (HDR-L-DED) technique have been carried out. To increase the material deposition rate, higher energy input is required. Tuominen et al. [1] used a 15 kW fibre laser to clad Inconel 625 with a powder deposition rate of 15.6 kg/h. A number of efforts have been made to integrate additional heat sources including electric arc or induction heating in laser cladding processes to increase the heat input for melting filler materials. Zeng et al. [2,3] combined laser cladding and induction heating to increase the heat input, in a laser induction hybrid cladding (LIHC) process to increase the deposition rate. At a powder feed rate of 75.6 g/min (mixed NiCrBSi and WC powder), a laser scanning speed of 2200 mm/min was achieved [4].

It should be noted that the powder utilisation efficiency in the studies introduced above was in the range of 60–80%. Therefore, there is room to increase powder utilisation efficiency to achieve higher

* Corresponding author.
*E-mail address:* lin.li@manchester.ac.uk (L. Li).

https://doi.org/10.1016/j.optlastec.2020.106280
Received 5 December 2019; Received in revised form 9 March 2020; Accepted 9 April 2020
Available online 16 April 2020
0030-3992/ 

effective deposition rates and less material waste. Researchers from Fraunhofer ILT developed an HDR-L-DED process with a powder utilisation efficiency of more than 90%, and the laser scanning speed was increased to 200 m/min by injecting the powder steam into the laser beam and melt them before they reached the substrate surface [5]. The principle was to increase the interaction time between powder stream and laser beam so that a higher temperature of powder particles could be obtained, making the powder particles more easily caught by the melt pool. Zhong et al. [6–8] investigated an HDR-L-DED process for the applications of cladding and additive manufacturing of IN718. Their studies included the influences of the processing parameters on the defect formation in the deposited layers [8], the relationship between powder stream characteristic and deposition quality [6], as well as the solidified material microstructure and properties [7,9]. Schopphoven et al. [5] optimised the process parameters of ultra-high-speed L-DED as a new coating technology. Their result showed that ultra-high-speed L-DED had the potential to be an alternative to hard chrome plating and thermal spraying for the application of wear and corrosion-resistant coating. However, the studies of using HDR-L-DED as an additive manufacturing process for multiple layer material deposition are few. In L-DED processes, the geometry of deposited track is an essential factor that affects the manufacturing resolution and the process parameters for multi-track or multi-layer deposition, including overlap distance and powder delivery nozzle to workpiece stand-off distance. A number of analytical models for both single track and multi-track deposition have been established to describe the track cross-sectional profile. They were conducted based on the track size measured after the deposition, which was not an online process. However, during the metal deposition, the track geometry is not uniform due to the heat accumulation or process fluctuation [10]. Calculating the track shape in real-time may help adjust the overlap distance or stand-off distance in real-time.

Compared with conventional L-DED processes, more heat accumulation and larger melt pool volume are generated in an HDR-L-DED process, resulting in lower manufacturing resolution and more unevenness. For additive manufactured components, especially those with large size or complex geometry, the issues of heat accumulation and process fluctuation will significantly influence the performance. As more molten materials are deposited, the influence of the added material on the melt pool dynamics is more significant. Accordingly, it is essential to monitor and control the process stability in HDR-L-DED processes. The most commonly monitored melt pool-related features during the L-DED processes are temperature and the dimensions.

For the temperature measurement, pyrometry and thermal imaging are usually applied. Bi et al. [11,12] presented a temperature-based process control method for an L-DED process. Since this work aimed to develop a closed-loop process control. Salehi and Brandt [13] used a two-colour pyrometer to measure the absolute temperature of the melt pool in the range of 800–2500 °C. Tang and Landers [14] developed an online melt pool temperature control process for L-DED. An IR pyrometer (Mikron Infrared MI-GA 5-LO) with a measurement range of 400–2500 °C was mounted on the powder feed nozzle to measure the melt pool temperature. Song and Mazumder [15] developed a pyrometry-based feedback control of the melt pool temperature during laser cladding processes. By integrating off-axial CCD cameras into this feedback control process, both the melt pool temperature and the clad height could be monitored and controlled [16]. Nassar et al. [17] developed an temperature-based intra-layer closed-loop control system for L-DED processes. A single-wavelength pyrometer was applied to measure the average temperature in a 4.5 mm diameter spot around the melt pool. Griffith et al. [18]. Investigated the thermal behaviour in the Laser Engineered Net Shaping (LENS) process with thermal imaging. A high-speed off-axial camera was applied to monitor the lateral view of the melt pool, and the temperature was obtained using a standard pyrometric technique. Wang et al. [19] developed a monitoring system to investigate the thermal process of LENS of stainless steel 410. A Si-based digital off-axial CCD camera was used to capture the side view of the melt pool, while a two-wavelength imaging pyrometer tracked the temperature at a dynamic range from 1450 °C to 1860 °C. Liu et al. [20] developed an optical monitoring process of high power laser cladding. A pyrometer with a temperature range from 470 °C to 3000 °C was applied to measure the temperature of the melt pool. An IR-camera (FLIR Thermovision A40) was used to record the melt pool temperature distribution. Khanzadeh et al. [21,22] carried out an investigation on predicting the porosity distribution in L-DED products. Muvvala et al. [23] investigated the thermal cycles with a pyrometer-based temperature measurement process in laser cladding of IN718, and a correlation between the thermal behaviour and the microstructure was established.

Vision-based monitoring processes have been developed to measure the melt pool dimensions. Hu and Kovacevic [24] developed a coaxial infrared (IR)-image sensing setup to monitor the melt pool during an L-DED process. An IR filter was mounted on a high-speed CCD camera, and the radiation wavelength of 700–1060 nm was received. The melt pool was identified based on the grey level distribution. Hofman [25] develop a coaxial camera-based melt pool monitoring system for laser cladding. A monochrome CMOS camera (PixeLINK PL-A741) was applied to measure the melt pool dimensions in real-time. Further, a feedback control was implemented based on the transient melt pool width. Ocylok et al. [26] studied the influence of the processing parameters on the melt pool geometry during L-DED by coaxial melt pool monitoring. A CMOS-camera was installed coaxially and recorded the back reflection of the melt pool. A sensing and control system was developed by Ding et al. [27] for a robotised L-DED process, where a coaxial CCD-camera was used to monitor the melt pool. The shape and the size of the melt pool was monitored to evaluate the process stability. Similar vision-based coaxial melt pool monitoring system was also reported by Vandone et al. [28]. High-speed cameras were also applied to analyse the melt pool dynamics in L-DED processes. Abe et al. [29] used an off-axial high-speed camera with a frame rate of 500 fps to investigate the track formation and the molten powder behaviour in a laser cladding process. Haley et al. [30] investigated the powder-melt pool impact in L-DED process. Four high-speed cameras (Photron SA-Z, Phantom V2512, Shimadzu HPV-2 and iX i-SPEED 720) were used to record the melt pool and powder flow field at a frames rate from 10 to 200 kHz. The powder-injection caused ripple on the melt pool surface was observed, as well as the floating particles. Wirth et al. [31] developed a coaxial monitoring system based on a high-speed camera (Vision Research Phantom v12.1) with a frame rate of 40,000–67,000 fps. By tracking the floating particles on the melt pool surface, the flow velocity field on the melt poo surface was reproduced.

For the vision-based monitoring system, the camera can be installed coaxially or off-axially to the laser beam. With an off-axial setup, the captured melt pool images are affected by the angle between the camera and the deposition direction. With a deposition pattern where the melt pool movement direction is not fixed, the angle between the camera and the deposition direction is changed. Hence, the image processing is more complicated. Meanwhile, the melt pool edge may be blocked by the already deposited track in the lateral view [32]. Although the use of multiple cameras can avoid this blocking effect [33,34], the cost and the complexity of the monitoring system are increased. On the other hand, only the top surface can be captured by the coaxial camera, and hence the track height cannot be obtained.

Despite various effort in the use of coaxial cameras for the monitoring of L-DED processes, little is known on the relationship between the observed images and the cross sectional profiles of the melt pool or the microstructural behaviour of solidified deposition. Furthermore, no reported work is seen on the coaxial visual inspection of HDR-L-DED processes.

In this paper, we show a coaxial in-situ imaging system for a high deposition rate L-DED process and a method to predict the cross-sectional profiles of both single track and multi-track deposition in real-time. Melt pool dynamics and relationship between melt pool

characteristic with material solidification grain growth properties are discussed. For the HDR-L-DED process which has a larger melt pool, a melt pool boundary fitting process is applied to estimate the melt pool size.

## 2. Experimental material and procedure

### 2.1. Experimental setup

Experiments were carried out using a coaxial HDR-L-DED imaging system through the deposition nozzle, with an IPG YLS-16000 continuous wave fibre laser having a maximum output power of 16 kW. The laser beam was delivered through an optical fibre with a core diameter of 300 μm and emitted from the end of the fibre. A lens collimated the beam with a 150 mm focal length was focused through a lens with a 400 mm focal length. The measured focus spot diameter was 0.8 mm. In this study, a defocused laser beam was set to obtain a large laser spot size. A deposition head (PRECITEC 0260) with a concentric powder feeding nozzle was connected to the laser head. The laser head with the deposition head was mounted on a 6-axis KUKA robot. The powder was delivered to the deposition head with a SULZER METCO TWIN 10-C powder feeder. Before the deposition process, the powder feed rate under different powder delivery parameters was measured. The deposition nozzle is shown in Fig. 1(a). Fig. 1(b–d) presents the transient powder stream and relative powder stream intensity distribution (Powder feed rate: 24 g/min, Carrier gas flow rate: 6 L/min).

Stainless steel (SS) 316L powder (from Höganäs Belgium) was applied as the deposition material in this study. The powders were spherical with a diameter range from 50 μm to 150 μm. The substrates used in this study were SS 316L flat sheets in a dimension of 100 mm × 100 mm × 10 mm. Before the deposition, the powder was dried in a vacuum drying cabinet at 120 °C for two hours. The parameters used in this experiment are listed in Table 1. The camera focus position affects the imaging quality. With different deposition parameters, although the height of the melt pool may vary, the melt pool edge is always on the substrate or the surface of previously deposited layer. Therefore, in this study, the camera was focused on the substrate or previously deposited layer, so that the boundary of the melt pool could be clearly observed even the melt pool dimension is different.

**Table 1**
Processing parameters applied in this study.

| Parameter | |
|---|---|
| Laser power (*LP*) | 3.5 kW |
| Travel speed (*TS*) | 10 mm/s |
| Powder feed rate (*PFR*) | 24 g/min |
| Carrier Ar gas flow rate | 6 L/min |
| Laser spot diameter ($D_L$) | 5 mm |
| Stand-off distance ($D_p$) | 11 mm |

Specimens, after the laser deposition, were cross-sectioned using electrical discharge machining (EDM). After grinding, polishing and electrolytic etching (5 V in 10% oxalic acid solution), the cross-sections of single track and multi-track were examined with a digital microscope (Keyence VHX-5000).

### 2.2. Acquisition and processing of melt pool transient images

A Phantom Miro 4 camera was applied to observe the melt pool during the deposition process. Both coaxial and off-axial cameras were installed in this study, as illustrated in Fig. 2(a, b). For the off-axial installation of the camera, an illumination laser source (from Oxford Lasers Ltd) was used to provide lighting for the high-speed imaging and a bandpass filter (from Edmund Optics) was mounted on the camera to filter off the interference light. With the off-axial configuration, the whole area of the melt pool was observed, as shown in Fig. 2(c). With

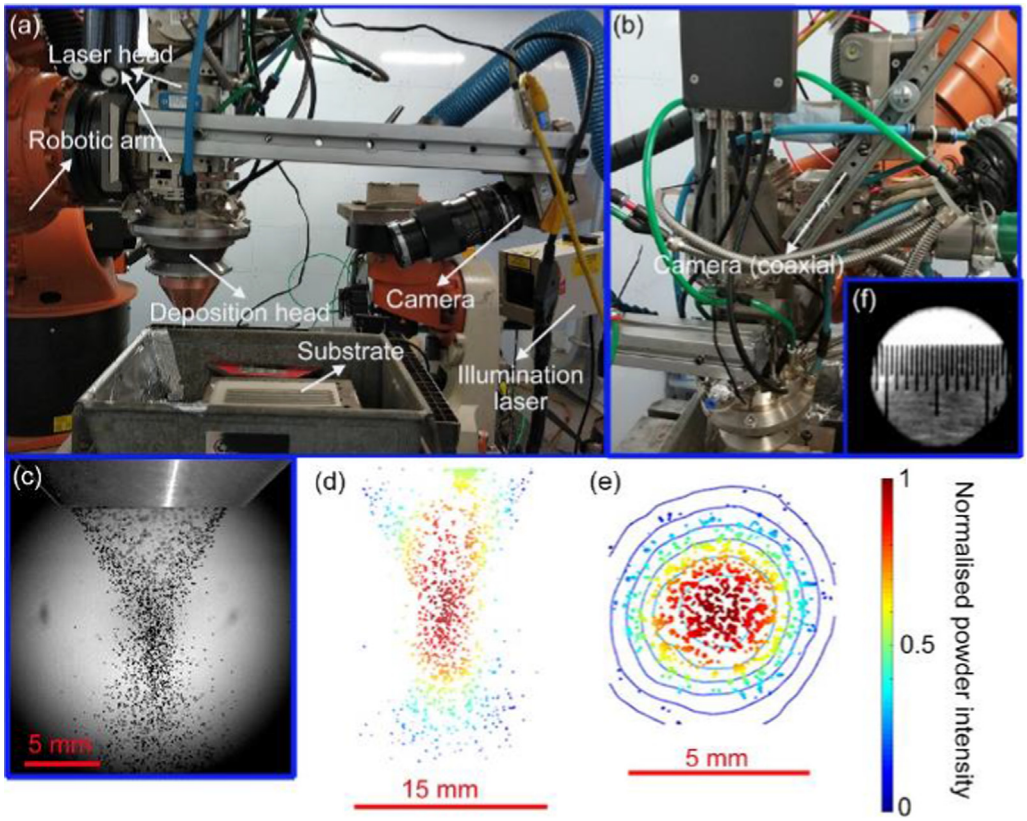


**Fig. 1.** The laser deposition head and powder stream intensity: (a) the set up for the off-axial camera; (b) the set up for the coaxial camera; (c) side view of the powder stream; (d) the transverse powder stream intensity; (e) the cross-sectional powder stream intensity and (f) the coaxial camera visual field.

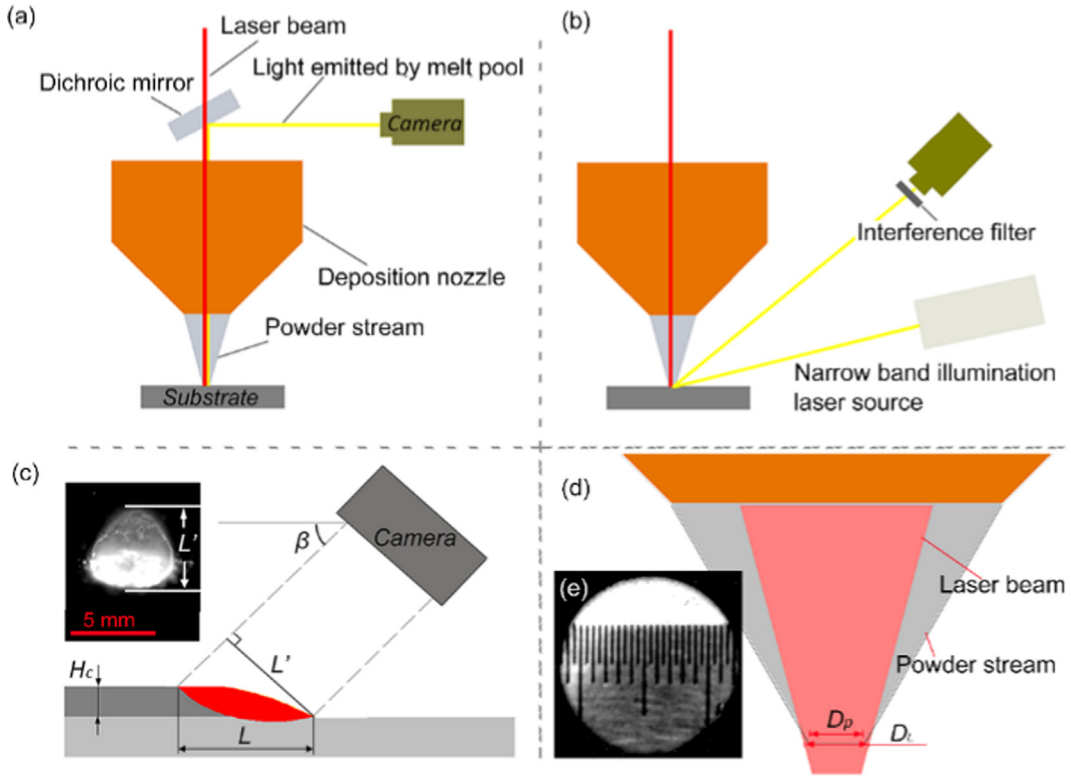


**Fig. 2.** Schematic setup of the imaging system: (a) coaxial camera installation; (b) off-axial camera installation; (c) melt pool morphology observed using off-axial imaging system; (d) illustration of laser beam and powder stream at processing area; (e) size of vision area through powder feeding nozzle.

the off-axially observed melt pool, the real length ($L$) of the melt pool can be calculated as

$$L = \frac{L^{'} - H_c\cos\beta}{\sin\beta} \tag{1}$$

where $L'$ is the measured melt pool length on the image, $H_c$ is the deposited track height and $\beta$ is the angle between the camera lens and deposition direction. As shown in Fig. 2(d), laser defocus position was applied to obtain a processing area with a diameter ($D_L$ = 5 mm) slightly larger than the powder stream converge diameter (around 4.5 mm). As the camera was mounted on the laser head for either coaxial or off-axial configuration, the motions of the camera and the processing position were synchronous. In the off-axial configuration, the camera was installed in front of the deposition head, as is illustrated in Fig. 1(a).

The camera installed coaxially to the laser beam was used to observe the processing area through the deposition nozzle central axis. The diameter of the vision area through the coaxial camera was around 13.5 mm (see Fig. 2(e)). By adjusting the focus position, aperture size and exposure time of the camera, the amount of the light that reached the camera was controlled. In this study, the camera focus position was adjusted at the processing plane, small aperture size and medium exposure time were selected to prevent overexposure of melt pool. Table 2 presents the parameters for melt pool imaging.

A captured melt pool image is shown in Fig. 3(a). As shown in Fig. 3(b), gamma correction was applied to enhance the greyscale gradient in the dark area on the melt pool snapshots, which is described in the following equation [35],

$$G_{out} = \lambda G_{in}^{\gamma} \tag{2}$$

where $G_{out}$ and $G_{in}$ are the output and input greyscale of a pixel, respectively, $\gamma$ is the power of the correction and $\lambda$ is a constant. The effect of the gamma correction ($\gamma$ = 0.3, $\lambda$ = 1) is shown in Fig. 3(b). A correction method was employed to remove the noise attributed from

**Table 2**
The parameters for melt pool imaging.

| | Parameter | Value & unit |
|---|---|---|
| coaxial | Exposure time | 30 us |
| | Frames per second | 100 |
| Off-axial | Camera lens-powder nozzle distance | 320 mm |
| | The angle between the camera lens and deposition direction | 30° |
| | Exposure time | 150 us |
| | Frames per second | 100 |
| Illumination laser source (for off-axial imaging) | Pulse duration | 10 μs |
| | Emitted wavelength | 808 nm |
| | Bandpass filter bandwidth | 810 ± 10 nm |

spatters, as expresses as:

$$G_{out} = \begin{cases} G_{in}, if G_{in} - G_M < G_T \\ G_M, if G_{in} - G_M \geq G_T \end{cases} \tag{3}$$

where $G_M$ is the median greyscale of the pixels in the surrounding area of a noise pixel and $G_T$ is a threshold greyscale difference to detect the noise pixels. In this study, the points within the distance of 10 pixels to the noise pixel were identified as the surrounding points and $G_T$ was set as 0. The effect of noise removal can be seen in Fig. 3(c). After the noise removal, the contrast of the melt pool was enhanced as is shown in Fig. 3(d). Then we used a fixed threshold greyscale 130 to find the melt pool, and the outermost melt pool pixels were recognised as the melt pool boundary. The extracted melt pool boundary is shown in Fig. 3(e).

Since the camera was installed coaxially with the laser beam, the visual field was limited by the powder nozzle exit diameter (13.5 mm). As for the deposition process, the melt pool size is larger, making it difficult to directly measure the melt pool length, as it is well beyond the viewing field as demonstrated in Fig. 4(a), where the green arc is the nozzle edge which blocks the tail part of the melt pool. In order to

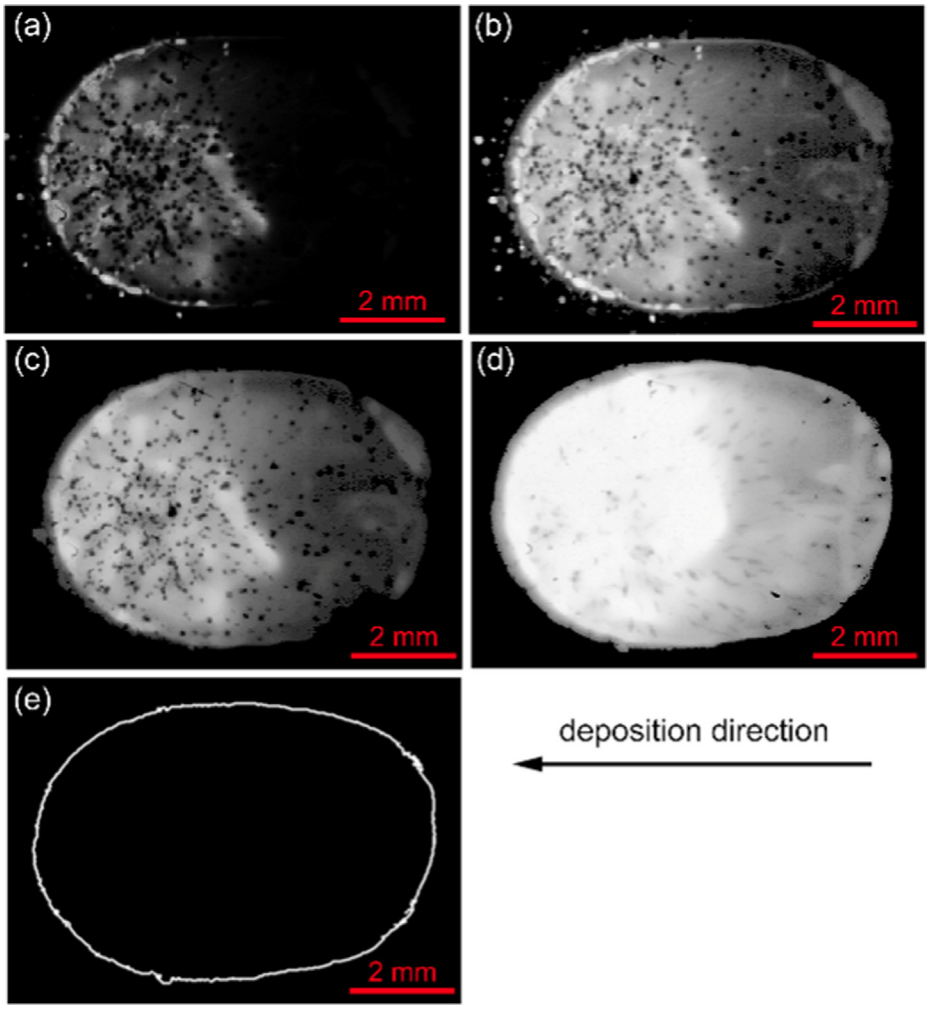


**Fig. 3.** The melt pool boundary extraction procedure: (a) original image; (b) gamma-corrected image; (c) noise-removed image; (d) contrast-enhanced image and (e) edge extraction of the melt pool.

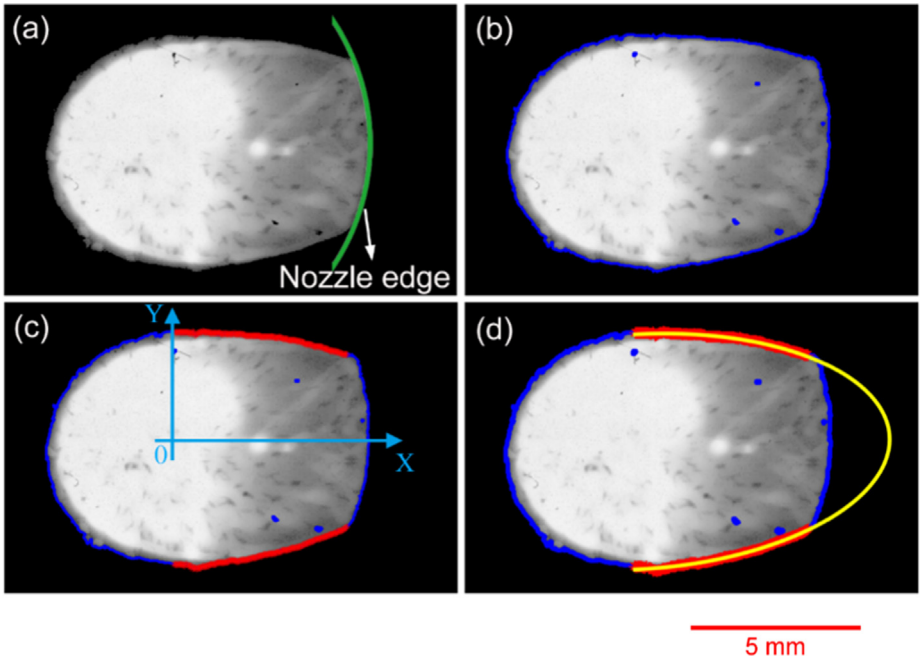


**Fig. 4.** An illustration of melt pool outline estimation procedure: (a) partially covered melt pool morphology; (b) edge extraction; (c) pixels extraction for curve fitting; (d) fitted melt pool shape.

obtain the melt pool length, a curve fitting algorithm was conducted to estimate the melt pool profile. In this study, the melt pool shape was assumed as an ellipse, and the fitting procedure is illustrated in Fig. 4.

As shown in Fig. 4(b), the observed melt pool edge was detected, and then part of the edge pixels located on the real melt pool boundary (marked in red in Fig. 4(c)) was extracted to be used to fit an ellipse to predict the profile of the sheltered part of the real the melt pool. A coordinate was established, where the origin was the laser spot centre. An ellipse can be expressed in the form of

$$Ax^2 + 2Bxy + Cy^2 + 2Dx + 2Ey + F = 0 \quad (4)$$

Here we used Taubin method to fit Eq. (4), and the implementation was given by Kanatani et al. [36,37]. The relative position between the camera and the deposition head was fixed. Thus, the position of the nozzle edge in each frame was unchanged. Therefore, the nozzle-edge points were predefined to be excluded from the fitting process. Fig. 4(d) shows the predicted melt pool shape.

In this study, a program was developed with a graphical language LabVIEW to perform the collecting and the processing of the images. The script of the image processing was created in MATLAB and it was invoked through the LabVIEW program. The program was run on a laptop computer (i7-7500 CPU @2.70 GHz, 16 GB RAM). The processing time for one frame was tested as 8.12 ms (averaged over 20 frames), which was shorter than the time interval (10 ms for 100 fps) of image acquisition.

### 2.3. Estimation of deposition track height based on transient melt pool size in real-time

With the measured melt pool width, the deposit height ($H_c$) can be estimated in real-time. For the estimation of $H_c$, the curve type of the cross-sectional outline requires to be assumed. Different kinds of shapes including parabolic [38–41], arc [42–47], sinusoidal [40] and elliptic [48] have been used for the fitting of bead cross-sectional profile in cladding process. Among these shapes, parabolic and arc are the most applied. Thus, in this study, these two curves were selected for the fitting of single-track cross-section.

By assuming the cross-sectional profile as parabolic and arc, the area ($A_c$) of track cross-section can be expressed by Eq. (5) for parabolic [39] and Eq. (6) for arc [43].

$$A_c = \frac{2WH_c}{3} \quad (5)$$

$$A_c = \frac{H_c}{3}\left(\frac{W}{2} + 4\sqrt{\frac{W^2 + 4H_c^2}{8} - \frac{H_c^2}{4}}\right) \quad (6)$$

According to the mass conservation of filler powder, with a given powder utilisation efficiency ($E_p$), the track cross-section area is presented as

$$A_c = \frac{PFR \times E_p}{\rho \times TS} \quad (7)$$

where ρ is the density of filler powder material (kg/m$^3$). By the simultaneous solving of Eqs. (5)–(7), the track height $H_c$ can be calculated. In general, the estimation of the track cross-section shape is used to calculate the cross-section area so that the powder utilisation efficiency can be obtained. As to estimate the track height, powder utilisation efficiency is required to be pre-set. Deposition trials were carried out to obtain the powder utilisation efficiency using the weighting method [49]. The measured $E_p$ was 0.9 ± 0.02, and for the calculation, 0.9 was employed as the value of $E_p$.

For multi-track-single-layer deposition, the cross-section of the deposited layer is illustrated in Fig. 5. The newly deposited track overlaps the previous track. Thus, the melt pool becomes partially inclined. It results in a change of layer height. A multi-track-single-layer model was built based on the work by Ocelík et al. [50,51]. As illustrated in Fig. 5,

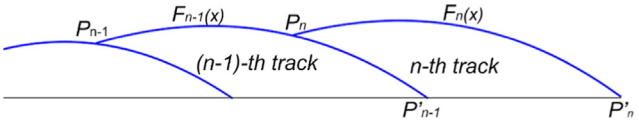


**Fig. 5.** A schematic representation of the adjacent tracks.

$F_n(x)$ indicates the function of the $n$-th track cross-sectional profile, $W_n$ is the measured melt pool width and $\Delta x$ is the overlap distance. Point $P_n=(n\Delta x-\frac{W_n}{2}, F_{n-1}(n\Delta x - \frac{W_n}{2})$ donates the intersection point of the $n$-th track and $(n-1)$-th track while $P_n^{'} = (n\Delta x + \frac{W_n}{2}, 0)$ is the intersection point of the $n$-th track and the substrate. Therefore, an equation set can be built as Eq. (8). The function of track cross-sectional outline can be obtained by solving Eqs. (7) and (8) (see Fig. 5).

$$\begin{cases} F_n(P_n) = F_{n-1}(P_n) \\ F_n(P_n^{'}) = 0 \\ A_{cn} = \int_{n\Delta x-\frac{W_n}{2}}^{n\Delta x+\frac{W_n}{2}} F_n dx - \int_{n\Delta x-\frac{W_n}{2}}^{(n-1)\Delta x-\frac{W_{n-1}}{2}} F_{n-1} dx \end{cases} \quad (8)$$

It was reported that in multi-track laser deposition, the powder utilisation efficiency was not a constant, but increasing gradually due to the increase of bulk substrate temperature [50,52]. Thus, a track number dependent correction of $E_p$ was adopted as

$$E_p = E_p + (n-1)\bullet\Delta \quad (9)$$

where $n$ is the number of deposited track and $\Delta$ is a coefficient that indicates the inclination of $E_p$. In the prediction model of cross-sectional profiles for multi-track-single-layer deposition, the substrate for the $n$-th track is the $(n-1)$-th track and the base plate. For multi-track-multi-layer deposition, the substrate for the predicted track is the previously deposited track and tracks in the previous layer. Hence, by including the area of previous layers under the integral segment, the cross-sectional profile of multi-track-multi-layer can be estimated [50].

## 3. Results and discussion

### 3.1. Accuracy of the melt pool size measurement

To analyse the measurement accuracy of melt pool width based on the imaging system, the width of the deposited track was experimentally measured, and a comparison between melt pool width and track width was made. The deposited track is slightly narrower than the melt pool width due to the shrinkage during solidification. In this study, this effect was minimal so that it was ignored. With given deposition parameters and image acquisition parameters, the corresponding position in the deposited track to an image can be located. The track widths at different positions (see Fig. 6) were measured using the three-

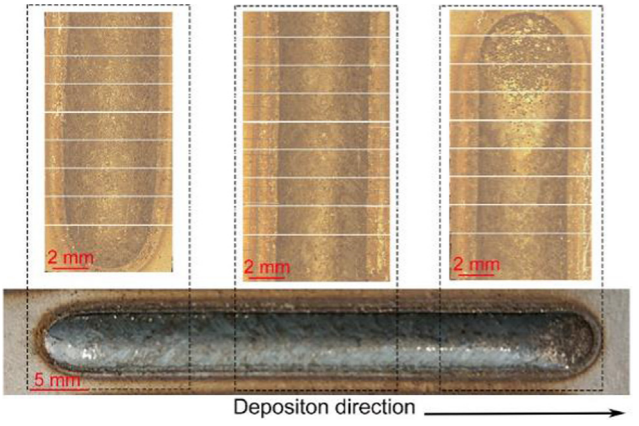


**Fig. 6.** Single deposited track and the measurement position using 3D scanning.

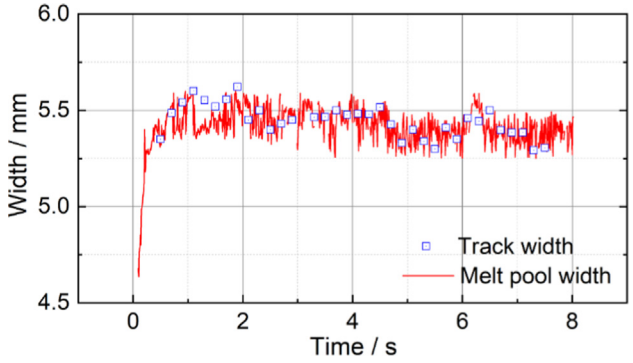


**Fig. 7.** The comparison of measured melt pool width and track width.

dimension (3D) scanning function of Keyence VHX-5000 digital microscope. Fig. 7 presents the comparison of the melt pool width and track width. It shows a good agreement between the melt pool width measured from the transient melt pool image and the deposit width measured by 3D scanning. The melt pool width started to increase after the laser was switched on and reached a stable value after about 0.5 s. 740 frames of melt pool were captured, and 35 positions of the deposited track were measured for validation. The standard deviation of the in-process measurement, in this case, was around 0.082 mm. In practice, average track width was applied to adjusting the overlap distance without considering the width fluctuation. The average width of the melt pool in the homogenous part of the track was about 5.41 mm while the average measured track width was about 5.32 mm, indicating an accuracy of more than 98% can be reached.

Fig. 8 shows the comparison of the transient melt pool length obtained by the estimation and experimental measurements. From the result, the melt pool kept increasing for 1.2 s after the laser was switched on, and then reached a stable value. The estimation accuracy in the melt pool length increasing stage (before 1.2 s) was good with an error of less than 0.4 mm. In the stable melt pool length stage, the estimation error was higher with a maximum error of 1.03 mm. The average melt pool length by the experimental measurement and estimation are 10.4 mm and 11.1 mm, respectively, which means an

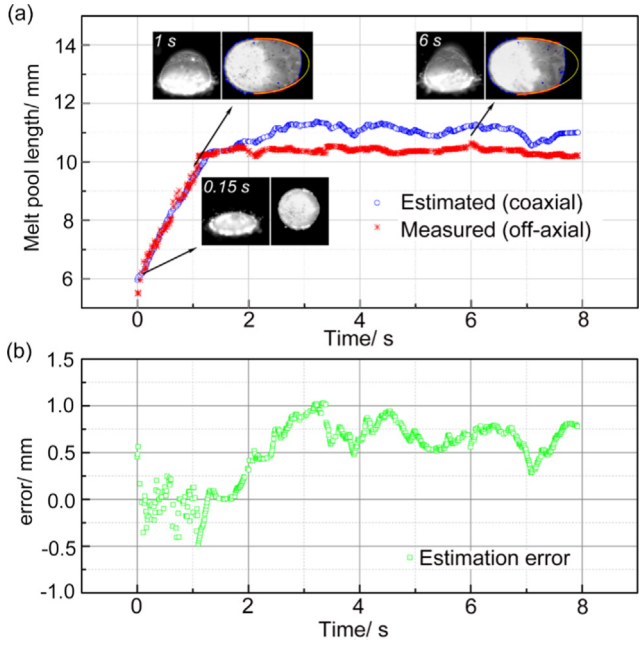


**Fig. 8.** The comparison of measured and estimated melt pool length: (a) measured and estimated melt pool length; (b) the error distribution of melt pool length estimation.

estimation accuracy of around 90% could be obtained.

### 3.2. Deposition height estimation based on the in-process measured melt pool width

To investigate the accuracy of the track height predicted in real-time. Single tracks with different parameters were deposited, and the cross-sections were fitted based on the real-time measured melt pool width. Fig. 9 presents the track cross-section and the fitted track profile. The track height of measured and the calculated track height are shown in Fig. 10. It is seen that the curvature of the track central area is smaller than the fitting curve of both parabolic and arc, while the curvature of the track cross-section near track root is greater. Therefore, the estimated height was greater than the real track height. As shown in Fig. 10, the error of track height estimation using parabolic for fitting was less than 6% while the maximum error of estimation using arc was 8%. Fig. 10 demonstrates that the fitting curves of parabolic and arc both well matched the track cross-sectional outline and using parabolic curve fitting one could obtain a better estimation result than using an arc. With a constant $E_p$, the intermixing of clad and substrate had no effects on the net volume of deposited tracks.

Layers with multi-track were deposited, as shown in Fig. 11, and the blue curves are the layer cross-sectional outlines calculated based on the melt pool width in real-time. Parabolic curves were selected as the fitting curves due to their higher accuracy for single-track fitting and faster calculating speed. Fig. 11(a–c) show the cross-sections and fitting curves of multi-track-single-layer with overlap percentage varies from 25% (4.5 mm) to 35% (3.9 mm). A good match can be obtained of the multi-track fitting with a small mismatch in the overlapping area of two adjacent tracks. In Fig. 11(d), a two-layer deposit (overlap percentage 35%, 7 tracks) is exhibited. For the case in this experiment, the gradual increase of $E_p$ was neglected as the correction coefficient Δ was 0. It is due to that in this deposition trial, and the generated melt pool width was 5.4 mm which was greater than the powder stream convergence diameter (see Fig. 1). A higher $E_p$ could be obtained initially, and the increase of melt pool size did not significantly influence $E_p$. This result was in agreement with the single track depositions (Figs. 9 and 10) for the single tracks with different deposition parameters, and the $E_p$ did not change remarkably. On the other hand, the relative stability of $E_p$ made the prediction reliable due to that the fluctuation of $E_p$ can be neglected.

### 3.3. Correlation between melt pool dynamics and melt pool geometry

It is well known that in a cladding or welding process, with different processing parameters, various crystal orientations are formed. They are formed based on the different heat gradients and solidification directions in the melt pool. According to solidification theory, the crystal morphology is governed by the normal velocity and thermal gradient in the local liquid. Therefore, knowledge of melt pool shape would be useful for predicting the crystal growth direction during the solidification of the melt pool. As the melt pool contour can be acquired in real-time, the solidification direction (crystal orientation) can be predicted in situ. Fig. 12 illustrates the procedure of generating the crystal growth direction from the aligned melt pool outlines. The aligned melt pool boundaries indicate the liquid isotherms. $M_n$ is a point on the $n$-th fitted melt pool boundary, and $L_n$ is the normal line of the outline through $M_n$. $M_{n+1}$ is the intersection point of $L_n$ and the $(n+1)$-th fitted curve, and $L_{n+1}$ is the normal line through $M_{n+1}$. To connect the intersection points, crystal orientation could be obtained. To simplify the calculation, the melt pool can be assumed as having a constant dimension when the deposition process reaches a steady state.

Figs. 13 and 14 show the comparisons of predicted solidification directions and experimental crystal orientations (from top view). The surface of the solidified track was observed without etching. The prediction agrees well with the observed result. With a travel speed (*TS*) of

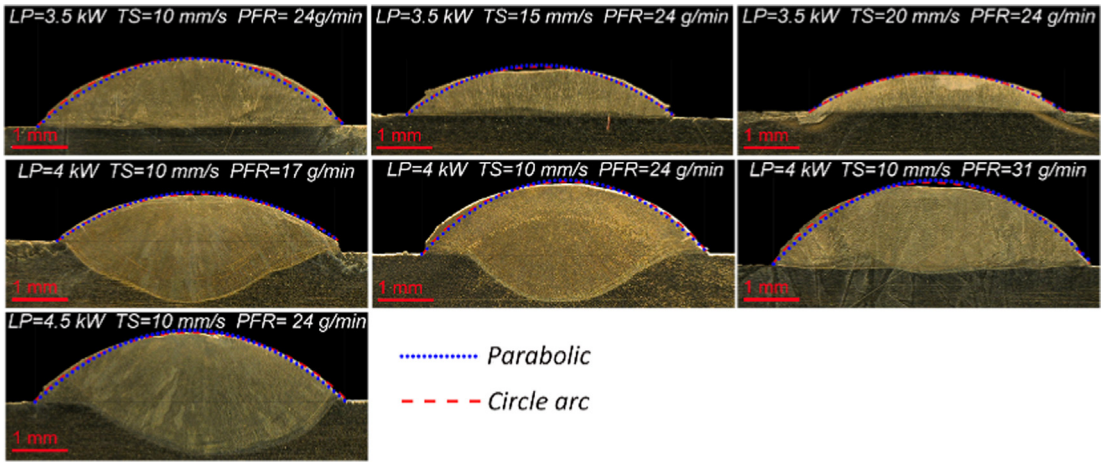


**Fig. 9.** Track cross-section and the fitted track profile.

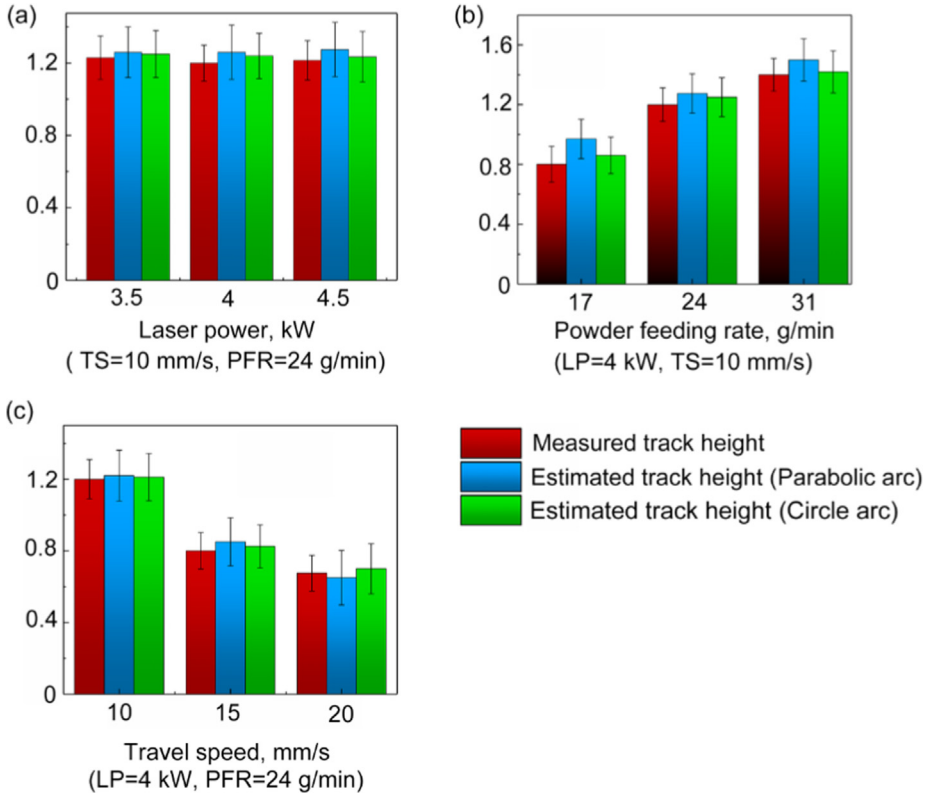


**Fig. 10.** Comparison of track height obtained by measurement and estimation: (a) track height with different laser power; (b) track height with different travel speed; (c) track height with different powder feed rate.

10 mm/s, the melt pool was in the shape of distorted ellipse, and the angle between the grain growth direction and deposition direction decreased from the track root to the central line. While with a higher *TS* of 20 mm/s, melt pool shape was more like a teardrop, the grain grew along a fixed direction. During the deposition process, the melt pool front end denoted the location where the melting was about to start, and the tail end of the melt pool denoted the area where solidification was over. The solidification front moved in a velocity $R_s = TS \times \cos\theta$, where $\theta$ is the angle between the solid-liquid interface normal orientation and the deposition direction. Therefore, based on the estimated melt pool shape, the solidification direction at the melt pool boundary can be obtained and thus the crystal morphology from the top view can be predicted in process.

The melt pool behaviour in the L-DED process is quite complicated due to the existence of turbulence. Besides, in this study, the melt pool behaviour is qualitative instead of quantitative. Basically, for the materials (ideal black body) with a melting point above 1000 K and vaporisation temperature above 3000 K, the spectral radiance is strong in the visible near-infrared range, which can be detected using conventional CCD or CMOS devices [53]. As for the real object that is not black body emitter, a value of emissivity is required to describe the comparison of the measured object to the black body. However, the emissivity is uncertain because it varies with temperature, emitted wavelength and surface condition. Measurements with more than one wavelength were used to avoid directly applying the Planck's law, and the temperature can be obtained by solving Eq. (10) [53].

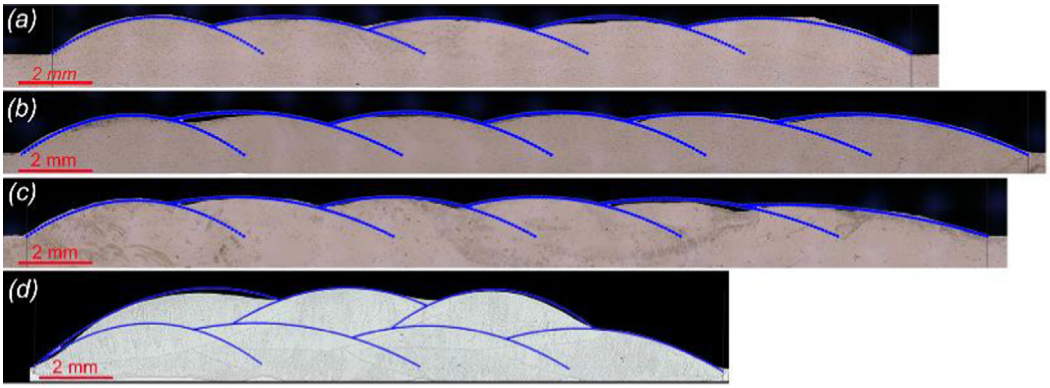


**Fig. 11.** Cross-sections of multi-track deposition and the fitting curves: (a) 5 tracks one layer, overlap percentage 25%; (b) 6 tracks one layer, overlap percentage 30%; (c) 6 tracks one layer, overlap percentage 35%; (d) 7 tracks two layers, overlap percentage 30%.

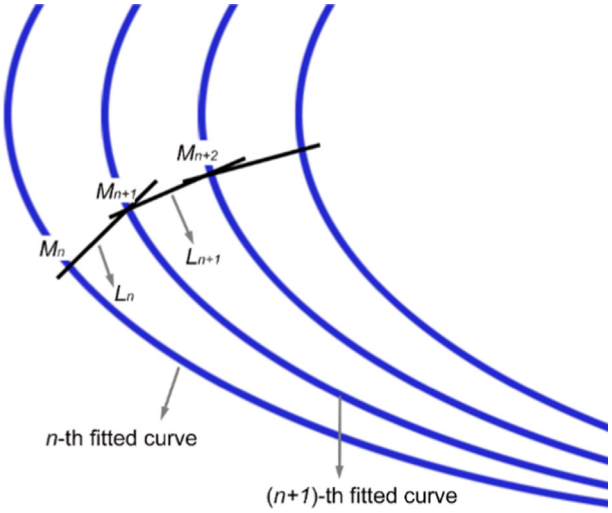


**Fig. 12.** Illustration of solidification direction through aligned melt pool boundaries.

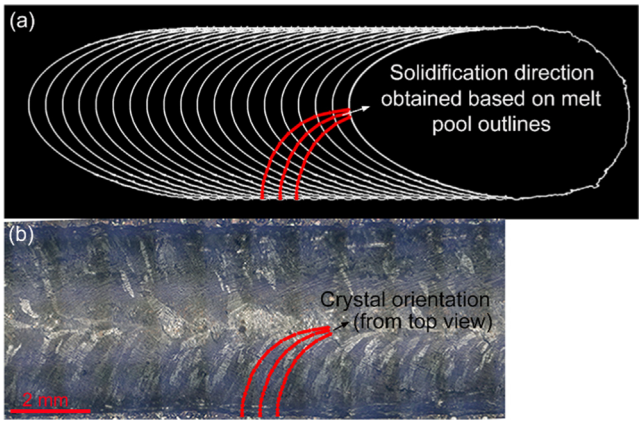


**Fig. 13.** Comparison of the predicted solidification rate and crystal orientation at a TS of 10 mm/s: (a) aligned melt pool outlines and solidification direction; (b) crystal orientation from the top view of the deposited track.

$$\frac{I_1}{I_2} = \frac{A_1\ \epsilon_1\ \lambda_2^5}{A_2\ \epsilon_2\ \lambda_1^5}\exp\left(\frac{h_c}{K_B}\frac{1}{T}\left(\frac{1}{\lambda_2} - \frac{1}{\lambda_1}\right)\right) \tag{10}$$

where $I_1$ and $I_2$ are intensities at wavelengths ??$_1$ and ??$_2$, A1 and A2 are the combined efficiencies at the applied wavelengths, $\epsilon_1$ and $\epsilon_2$ are the emissivity, $h_c$ is the Planck's constant and $k_B$ is the Boltzmann's constant. For the camera used in this study, the temperature cannot be reliably measured. As for further research, multiply wavelengths measurement is to be made to obtain the temperature field of the melt pool.

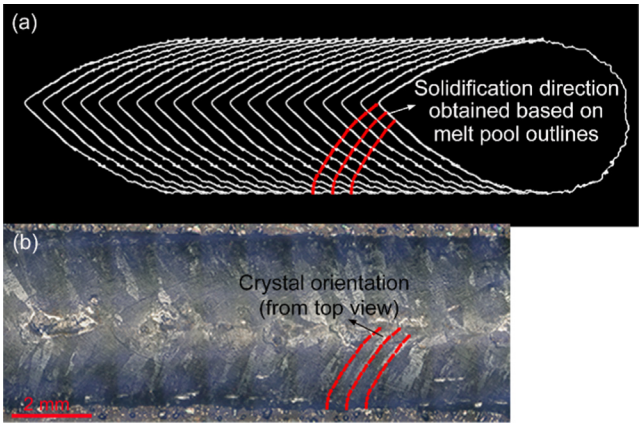


**Fig. 14.** Comparison of the predicted solidification rate and crystal orientation at a TS of 20 mm/s: (a) aligned melt pool outlines and solidification direction; (b) crystal orientation from the top view of the deposited track.

## 4. Conclusions

To observe the melt pool characteristics in real-time in a HDR L-DED process, a coaxial imaging system has been utilised. The morphology of the melt pool and the cross sectional dimension of the solidified track and grain structures of the solidified tracks were predicted. The conclusions of this work are drawn as:

(1) A sharp melt pool edge was obtained. The measured melt pool width of the homogenous part of the track can reach an accuracy that is higher than 98%.
(2) A curve fitting method was applied to estimating the melt pool shape partially blocked by the deposition nozzle from the coaxial viewing camera. The error of the estimated melt pool length was less than 10%.
(3) Based on the obtained melt pool shape parameters, a new approach to predict the cross-sectional profile of the deposited track was introduced. For both single track and multi-track, a good match between the predicted and real cross-section was achieved.
(4) The obtained melt pool shape has a relationship with the heat transfer and mass flow in the melt pool. The melt pool boundary shape can predict the crystal growth direction.

## Declaration of Competing Interest

The authors declare that they have no known competing financial interests or personal relationships that could have appeared to influence the work reported in this paper.

## References


[1] J. Tuominen, J. Näkki, H. Pajukoski, T. Peltola, P. Vuoristo, High deposition rate laser cladding: recent advancements, in: 5th Annual Laser Additive Manufacturing (LAM) Workshop. Houston, 2013.

[2] Y. Huang, X. Zeng, Q. Hu, Analysis of laser-induction hybrid cladding processing conditions, in: Library, 2007, p. 1–8.

[3] L. Meng, K. Hou, D. Wang, Q. Hu, X. Zeng, C. Xian, Microstructure and mechanical properties of the coatings in laser cladding and laser-induction hybrid cladding of full-scale rail, Adv. Laser Process. Manuf. II (2018) 48.

[4] S. Zhou, X. Dai, Laser induction hybrid rapid cladding of WC particles reinforced NiCrBSi composite coatings, Appl. Surf. Sci. 256 (14) (2010) 4708–4714.

[5] T. Schopphoven, A. Gasser, K. Wissenbach, R. Poprawe, Investigations on ultra-high-speed laser material deposition as alternative for hard chrome plating and thermal spraying, J. Laser Appl. 28 (2) (2016).

[6] C. Zhong, N. Pirch, A. Gasser, R. Poprawe, J. Schleifenbaum, The influence of the powder stream on high-deposition-rate laser metal deposition with Inconel 718, Metals (Basel) 7 (10) (2017) 443.

[7] C. Zhong, A. Gasser, J. Kittel, K. Wissenbach, R. Poprawe, Improvement of material performance of Inconel 718 formed by high deposition-rate laser metal deposition, in: Materials and Design. Elsevier Ltd, 2016, pp. 128–134.

[8] C. Zhong, T. Biermann, A. Gasser, R. Poprawe, Experimental study of effects of main process parameters on porosity, track geometry, deposition rate, and powder efficiency for high deposition rate laser metal deposition, J Laser Appl. 27 (4) (2015) 042003.

[9] S. Sui, C. Zhong, J. Chen, A. Gasser, W. Huang, J.H. Schleifenbaum, Influence of solution heat treatment on microstructure and tensile properties of Inconel 718 formed by high-deposition-rate laser metal deposition, J. Alloys Compd. 740 (2018) 389–399.

[10] S.M. Saqib, Experimental Investigation of Laser Cladding Bead Morphology and Process Parameter Relationship for Additive Manufacturing Process Characterization - PhD Dissertation. University of Windsor, 2016.

[11] G. Bi, A. Gasser, K. Wissenbach, A. Drenker, R. Poprawe, Characterization of the process control for the direct laser metallic powder deposition, Surf. Coat. Technol. 201 (6) (2006) 2676–2683.

[12] G. Bi, A. Gasser, K. Wissenbach, A. Drenker, R. Poprawe, Investigation on the direct laser metallic powder deposition process via temperature measurement, Appl. Surf. Sci. 253 (2006) 1411–1416.

[13] D. Salehi, M. Brandt, Melt pool temperature control using LabVIEW in Nd : YAG laser blown powder cladding process, Int. J. Adv. Manuf. Technol. 29 (2006) 273–278.

[14] L. Tang, R.G. Landers, Melt pool temperature control for laser metal deposition processes— art I: online temperature control, J. Manuf. Sci. Eng. 132 (2015) 1–9.

[15] L. Song, J. Mazumder, Feedback control of melt pool temperature during laser cladding process, IEEE Trans. Control Syst. Technol. 19 (6) (2011) 1349–1356.

[16] L. Song, V. Bagavath-Singh, B. Dutta, J. Mazumder, Control of melt pool temperature and deposition height during direct metal deposition process, Int. J. Adv. Manuf. Technol. 58 (2012) 247–256.

[17] A.R. Nassar, J.S. Keist, E.W. Reutzel, T.J. Spurgeon, Intra-layer closed-loop control of build plan during directed energy additive manufacturing of Ti–6Al–4V, Addit. Manuf. 6 (2015) 39–52.

[18] M.L. Griffith, M.E. Schlienger, L.D. Harwell, M.S. Oliver, M.D. Baldwin, M.T. Ensz, et al., Understanding thermal behavior in the LENS process, Mater. Des. 20 (1999) 107–113.

[19] L. Wang, S.D. Felicelli, J.E. Craig, Thermal Modeling and Experimental Validation in the LENS Process, in: 18th International Solid Freeform Fabrication Sympo- sium. Austin, TX, 2007, pp. 100–111.

[20] S. Liu, P. Farahmand, R. Kovacevic, Optical monitoring of high power direct diode laser cladding, Opt. Laser Technol. 64 (2014) 363–376.

[21] M. Khanzadeh, S. Chowdhury, M.A. Tschopp, H.R. Doude, M. Marufuzzaman, L. Bian, In-situ monitoring of melt pool images for porosity prediction in directed energy deposition processes, IISE Trans. (2018) 1–19.

[22] M. Khanzadeh, L. Bian, N. Shamsaei, S.M. Thompson, Porosity Detection of Laser Based Additive Manufacturing Using Melt Pool Morphology Clustering, In: Proceedings of the 26th Annual International Solid Freeform Fabrication Symposium, 2016, pp. 1487–1494.

[23] G. Muvvala, D.P. Karmakar, A. Kumar, Online monitoring of thermo-cycles and its correlation with microstructure in laser cladding of nickel based super alloy, Opt. Lasers Eng. 88 (2017) 139–152.

[24] D. Hu, R. Kovacevic, Sensing, modeling and control for laser-based additive manufacturing, Int. J. Mach. Tools Manuf. 43 (1) (2003) 51–60.

[25] J. Hofman, Development of an observation and control system for industrial laser cladding, University of Twente, 2009.

[26] S. Ocylok, E. Alexeev, S. Mann, A. Weisheit, K. Wissenbach, Kelbassa I. Correlations of melt pool geometry and process parameters during laser metal deposition by coaxial process monitoring, Phys. Proc. (56C) (2014) 228–238.

[27] Y. Ding, J. Warton, R. Kovacevic, Development of sensing and control system for robotized laser-based direct metal addition system, Addit. Manuf. 10 (2016) 24–35.

[28] A. Vandone, S. Baraldo, A. Valente, F. Mazzucato, A. Valente, F. Mazzucato, et al., Vision-based melt pool monitoring system setup for additive manufacturing May, Proc. CIRP 81 (2019) 747–752.

[29] N. Abe, D. Tanigawa, M. Tsukamoto, Y. Hayashi, H. Yamazaki, Y. Tatsumi, et al., Dynamic observation of formation process in laser cladding using high speed video camera, ICALEO 2013 (2013).

[30] J.C. Haley, J.M. Schoenung, E.J. Lavernia, Observations of particle-melt pool impact events in directed energy deposition, Addit. Manuf. 22 (2018) 368–374.

[31] F. Wirth, S. Arpagaus, K. Wegener, Analysis of melt pool dynamics in laser cladding and direct metal deposition by automated high-speed camera image evaluation, Addit. Manuf. 21 (January) (2018) 369–382.

[32] L. Song, F. Wang, S. Li, X. Han, Phase congruency melt pool edge extraction for laser additive manufacturing, J. Mater. Process. Technol. 250 (July) (2017) 261–269.

[33] M. Asselin, E. Toyserkani, M. Iravani-tabrizipour, A. Khajepour, Cam CAD, Development of Trinocular CCD-Based Optical Detector for Real-Time Monitoring of Laser Cladding, in: Proceedings of the IEEE International Conference on Mechatronics & Automation. Niagara Falls, 2005, pp. 1190–1196.

[34] M. Iravani-Tabrizipour, E. Toyserkani, An image-based feature tracking algorithm for real-time measurement of clad height, Mach. Vis. Appl. 18 (2007) 343–354.

[35] David Travis, Effective Color Displays: Theory and Practice, Academic Press, London, 1991, p. 301.

[36] K. Kanatani, P. Rangarajan, Hyper least squares fitting of circles and ellipses, Comput. Stat. Data Anal. 55 (6) (2011) 2197–2208.

[37] K. Kanatani, Y. Sugaya, Y. Kanazawa, Guide to 3D, Vision Comput. (2016) 11–33.

[38] S. Suryakumar, K.P. Karunakaran, A. Bernard, U. Chandrasekhar, N. Raghavender, D. Sharma, Weld bead modeling and process optimization in Hybrid Layered Manufacturing, CAD Comput. Aided Des. 43 (4) (2011) 331–344.

[39] M.R. Boddu, S. Musti, R.G. Landers, S. Agarwal, F. Liou, Empirical modeling and vision based control for laser aided metal deposition process, Proc. 12th Annu. Int. Solid Free Fabr. Symp. (2001) 452–459.

[40] J. Xiong, G. Zhang, H. Gao, L. Wu, Modeling of bead section profile and overlapping beads with experimental validation for robotic GMAW-based rapid manufacturing, Robot Comput. Integr. Manuf. 29 (2) (2013) 417–423.

[41] Y. Cao, S. Zhu, X. Liang, W. Wang, Overlapping model of beads and curve fitting of bead section for rapid manufacturing by robotic MAG welding process, Robot Comput. Integr. Manuf. 27 (3) (2011) 641–645.

[42] W. Ya, Laser Materials Interactions During a Nalyses on Clad Formation, Thermal Cycles, The University of Twente, Residual, 2015.

[43] S.J. Davis, K.G. Watkins, G. Dearden, E. Fearon, J. Zeng, Optimum deposition parameters for the direct laser fabrication (DLF) of quasi-hollow structures, in: Proceedings of Photon Conference Manchester, Institute of Physics. Manchester, 2006.

[44] W. Aiyiti, W. Zhao, B. Lu, Y. Tang, Investigation of the overlapping parameters of MPAW-based rapid prototyping, Rapid Prototyp. J. 12 (3) (2006) 165–172.

[45] C. Lalas, K. Tsirbas, K. Salonitis, G. Chryssolouris, An analytical model of the laser clad geometry, Int. J. Adv. Manuf. Technol. 32 (1–2) (2007) 34–41.

[46] H. El Cheikh, B. Courant, J.Y. Hascoët, R. Guillén, Prediction and analytical description of the single laser track geometry in direct laser fabrication from process parameters and energy balance reasoning, J. Mater. Process. Technol. 212 (9) (2012) 1832–1839.

[47] H. El Cheikh, B. Courant, S. Branchu, J.Y. Hascoët, R. Guillén, Analysis and prediction of single laser tracks geometrical characteristics in coaxial laser cladding process, Opt. Lasers Eng. 50 (3) (2012) 413–422.

[48] Billy Chan, M.B. Jack Pacey, Modelling gas metal arc weld geometry usingartificial neural network technology, Can Metall Q. 38 (1) (1999) 43–51.

[49] K. Zhang, X.M. Zhang, W.J. Liu, Influences of processing parameters on dilution ratio of laser cladding layer during laser metal deposition shaping, Adv. Mater. Res. 549 (2012) 785–789.

[50] V. Ocelík, O. Nenadl, A. Palavra, J.T.M. De Hosson, On the geometry of coating layers formed by overlap, Surf. Coat. Technol. 242 (2014) 54–61.

[51] O. Nenadl, W. Kuipers, N. Koelewijn, V. Ocelík, J.T.M. De Hosson, A versatile model for the prediction of complex geometry in 3D direct laser deposition, Surf. Coat. Technol., 307 (2016) 292–300.

[52] S. Sun, M. Brandt, J. Harris, Y. Durandet, The influence of stellite 6 particle size on the inter-track porosity in multi-track cladding, Surf. Coat. Technol. 201 (3–4) (2006) 998–1005.

[53] P.A. Hooper, Melt pool temperature and cooling rates in laser powder bed fusion, Addit. Manuf. 22 (May) (2018) 548–559.